Biosystems Engineering, Vol. 167, March 2018, pp. 144-158
DOI:10.1016/j.biosystemseng.2018.01.004

Hyperspectral measurements of yellow rust and fusarium head blight in cereal crops: Part 2: On-line field measurement

Rebecca L Whetton[a], Toby W Waine[a], and Abdul M Mouazen[a,b]*

[a]Cranfield Soil and AgriFood Institute, Cranfield University, Bedfordshire MK43 0AL, UK.

[b] Department of Soil Management, Ghent University, Coupure 653, 9000 Gent, Belgium.

E-mail of corresponding author: Abdul.Mouazen@UGent.be

Abstract

Yellow rust and fusarium head blight cause significant losses in wheat and barley yields. Mapping the spatial distribution of these two fungi diseases at high sampling resolution is essential for variable rate fungicide application (in case of yellow rust) and selective harvest (in case of fusarium head blight). This study implemented a hyperspectral line imager (spectrograph) for on-line measurement of these diseases in wheat and barley in four fields in Bedfordshire, the UK. The % coverage was assessed based on two methods, namely, infield visual assessment (IVA) and photo interpretation assessment (PIA) based on 100-point grid overlaid RGB images. The spectral data and disease assessments were subjected to partial least squares regression (PLSR) analyses with leave-one-out cross-validation. Results showed that both diseases can be measured with similar accuracy, and that the performance is better in wheat, as compared to barley. For fusarium, it was found that PIA analysis was more accurate for on-line measurement than IVA. The prediction accuracy obtained with PIA was classified as good to moderately accurate, since residual prediction deviation (RPD) values were 2.27 for wheat and 1.56 for barley, and R^2 values were 0.82 and 0.61, respectively.

Similar results were obtained for yellow rust but with IVA, where model performance was classified as moderately accurate in barley (RPD = 1.67, R^2 = 0.72) and good in wheat (RPD = 2.19, R^2 = 0.78). It is recommended to adopt the proposed approach to map yellow rust and fusarium head blight in wheat and barley.

Keywords

On-line measurement, yellow rust, fusarium head blight, wheat, barley, mapping, partial least squares regression.

1. Introduction

Site specific fungi disease control is a large task for successful production of cereals worldwide, and requires data sampled at high spatial resolution due to in-field variation of these diseases. The severity of these diseases depends mainly on weather conditions, which necessitates information not only on disease spread, but weather conditions too. Yellow rust (*Puccinia . striiformis*) is a foliar disease that is common in cool climates, and is one of the most devastating diseases of wheat worldwide, reducing crop yields by up to 7 tonne ha^{-1} in severe epidemics (Ma *et al.,* 2001; Bravo *et al.,* 2003). In 2009 yellow rust mutations have enabled the disease to attack several widely grown genetically resistant cereal crop varieties, including Solstice (Milus *et al.,* 2009). Another important fungal disease that attacks cereal crops is fusarium head blight, with the most aggressive and prevalent species (*Fusarium graminearum*), causing mycotoxins in the grain (Desjardin, 2006; Brennan *et al.,* 2003; Leslie and Summerell, 2006; Rotter *et al.,* 1996). Fusarium predominantly affects the ear of the crop and has become one of the most important pre-harvest diseases worldwide. Like yellow rust, fusarium head blight also causes reduction in yield quantity and quality and when producing mycotoxins it becomes a significant threat to both humans and animals. Fusarium head blight is a sporadic disease, that is

49 dependent on warm humid weather conditions (Rossi *et al.,* 2001; Xu, 2003), causing variability of
50 disease presence and level of infection across regions, and years (Jelinek *et al.,* 1989). Both yellow
51 rust and fusarium species can survive in soil and weeds occurring in the hedgerows and borders of a
52 field, and fusarium head blight also survives within plant residues even after 2 years, acting as a
53 source of inoculum (Imathiu *et al.,* 2013; Jenkinson and Parry, 1994; Champeil *et al.,* 2004).
54 Therefore, control of mycotoxins caused by fusarium fungi is required to prevent toxic contamination
55 reaching the food chain either in milling grain (for human consumption) or as cattle feed (Magan *et*
56 *al., 200*2).

57 Traditionally, disease detection is carried out manually by human experts using visual assessments of
58 disease coverage throughout the field, a process that can be lengthy, subjective and tiresome (Schmale
59 and Bergstrom, 2003; Bock *et al.,* 2010). This method is limited in providing high sampling resolution
60 data on spatial variability of crop disease. Therefore, on-line mobile systems are necessary to inform
61 site specific application of fungicides.

62 It has been stated that optical technologies are available for development into suitable disease
63 detection systems, but with many challengers still required to be overcome (West *et al.,* 2003).
64 Although on-line applications are still rather limited, optical techniques have the potential to be
65 integrated with agricultural vehicles. Optical (both remote and proximal) methods can provide non-
66 invasive, high sampling resolution data that are necessary for monitoring and mapping of crop
67 diseases. Among optical sensing methods, hyperspectral and multispectral imaging techniques are
68 among the best candidates, as they have been used in disease and stress monitoring (Hahn, 2009).
69 Non-mobile (off-line) field and laboratory methods for disease classification and plant growing
70 conditions have been studied and demonstrated (Roggo *et al.,* 2003; Wu *et al.,* 2008). The early
71 success in field studies for hyperspectral image-based detection of yellow rust (Moshou *et al.,* 2004
72 and Bravo *et al.,* 2003) focused on the presence of yellow rust in the field, not necessarily the
73 severity. Moshou *et al.,* (2005) implemented a data fusion approach of a hyperspectral (450-900 nm)
74 and fluorescence (550-690 nm) imaging techniques for yellow rust detection in winter wheat,

reporting 94.5% accuracy. Other common attempts with hyperspectral and multispectral imagery are targeted to leaves rather than the canopy (Bock *et al.,* 2010). Huang *et al.* (2015) successfully provided quantitative assessment of yellow rust in winter wheat, by hyperspectral measurement of individual infected leaves. Zhou *et al.* (2015) used low cost RGB images for quantification of yellow rust, reporting 74% and 81% detection accuracies. Zhao *et al.* (2016) focused on two sensitive bands (558 nm and 856 nm) in the wavelength ranges of 550-680 nm and 750-1300 nm to detect yellow rust with 90.6% accuracy. Krishna *et al.* (2014) used remote hyperspectral data in 350 to 2500 nm range for quantitative identification of yellow rust. To the best of our knowledge there are no reports in the literature on on-line application of proximally captured hyperspectral imagery for simultaneous assessment and mapping of yellow rust and fusarium head blight in wheat and barley. Such analyses in laboratory conditions was discussed in Part 1 of this study (Whetton *et al.,* 2017b), where plants in trays were subjected to variable water stress, and were inoculated with yellow rust and fusarium head blight. The aim of this paper is to implement a hyperspectral imager for on-line measurement of yellow rust and fusarium head blight in wheat and barley grown commercially outdoors in the fields.

2. Materials and methods

2.1. Field sites

Field measurements were conducted in four different field sites through the 2015 cropping season. These sites were located at Duck End farm, Wilstead, Bedfordshire, UK (52°05'46.3"N 0°26'41.4"W), with an average annual rainfall of 598 mm. The farm has a three year crop rotation of oil seed rape, winter wheat and winter barley. Fields varied in size between 12, 10, 7 and 4 ha (Table 1), to allow for pattern identification of diseases with different field size. This is because yellow rust and fusarium head blight occurrence in the field often begins nearer the hedgerows, and the spread pattern throughout the growing season may well depend on the shape and size of the field. Winter wheat was grown in three fields, whereas winter barley was grown in the 10 ha field only. The largest and smallest winter wheat fields were scanned at two different intervals. Timing and growth stage of measurement in each field is shown in Table 1. Growth stage in this study refers to the Zadok's scale

101 (Zadoks *et al.,* 1974). The dominant soil texture types in the fields are shown in Table 1, with sand
102 fractions due to underlying gravel deposits.

103 **2.2. Soil moisture content measurement**

104 An on-line visible and near infrared (vis-NIR) spectroscopy soil sensor developed by Mouazen (2006)
105 was used in this study to measure gravimetric soil moisture content (MC) in field 4, with the objective
106 of studying the influence of MC on crop disease spatial distribution. The system consists of a
107 subsoiler, opening a smooth trench at 15 cm depth (Mouazen *et al.,* 2005). The sensor was mounted
108 on a three-point linkage of a tractor travelling at a speed of 3 km h^{-1} and collecting soil spectral data at
109 10 m parallel intervals. In order to measure soil spectra an AgroSpec mobile, fibre type, vis–NIR
110 spectrophotometer (Tec5 Technology for Spectroscopy, Oberursel, Germany), with a measurement
111 range of 305–2200 nm and a light source of 20W tungsten halogen lamp were used (Kuang &
112 Mouazen, 2013). A DGPS (EZ-Guide 250, Trimble, California, USA) recorded the position of the on-
113 line spectra with sub-meter accuracy. The collection of soil spectra and DGPS readings took place at 1
114 sec sampling resolution using AgroSpec software (Tec5 Technology for Spectroscopy, Oberursel,
115 Germany). A previously developed MC PLSR model (Halcro *et al.,* 2013) was used to predict MC
116 based on on-line collected spectra in the field.

117 **2.3. Hyperspectral on-line data capture**

118 In this study the term 'on-line' refers to a mobile measurement system, attached to a moving platform
119 (e.g., a tractor), where spectral data is captured whilst the platform is in motion, whereas 'non-mobile'
120 is defined as capturing the hyperspectral data in a stationary position. A push broom hyperspectral
121 imager (spectrograph) (HS spectral camera model from Gilden Photonics Ltd., UK) and light source
122 were mounted on a tractor by means of a metal frame (Figure 1). Optimal hyperspectral measurement
123 configurations set by Whetton *et al.* (2017a) were considered in the design and manufacturing of this
124 on-line measurement system of crop canopy. These include an integration time of 50 ms, a camera
125 height of 0.3 m and light height and distance of 1.2 m and a camera angle of 10°. The on-line
126 measurements were carried out at a travel speed of approximately 4 km h^{-1}. Sampling resolution was 1

127 Hz, which is subsequently logged and geo-located with sub-meter accuracy, using a differential global
128 positioning system (DGPS) (EZ-Guide 250, Trimble, California, USA). The direction and angle of the
129 imager was kept consistent, and a day with uniformly overcast weather was selected, which helped
130 prevent issues of moving shadows from lateral sun movement on the data (West *et al.,* 2003).

131 The same hyperspectral imager used in Part 1 of this study was used for on-line field measurement,
132 along with two external halogen lamps. It consists of 1608 pixels, with a spectral range of 400 - 1000
133 nm. More details about the hyperspectral imager's properties can be found in Whetton *et al.* (2017a).
134 In order to compile a full image from a set of line imagery, a steady moving platform is needed to
135 sweep across the target object to capture every line (Gilden Photonics Ltd, Glasgow, UK). However,
136 due to practical constraints of applying a consistent moving platform, the spectraSENS v3.3 software
137 (Gilden Photonics Ltd, Glasgow, UK) was adapted to record a single line array. Before data capture, a
138 white and dark reference were collected, and subsequently repeated at 10 minute intervals until the
139 scanning was completed. The white reference used was a commercially available Spectralon Teflon
140 white reflectance panel with 99.9% reflectance value. The collected on-line data was corrected by the
141 white and dark scans after data collection was complete, providing the relative reflectance.

142 **2.4. Disease recognition in the field**

143 During field scans with the hyperspectral imager, ground truth locations were selected randomly, at a
144 rate of five samples per hectare (Figure 2), and a set of five hyperspectral images were collected per
145 ground truth location, covering 1 m² plot. The measurement position was recorded with a DGPS. The
146 disease assessment was assigned to each of the five scans. In order to assist in disease and crop health
147 assessments , a photograph was collected at each position using an RGB, 5 megapixel camera with a
148 3.85 mm f/2.8 lens at the same time of hyperspectral image capture. The 1 m² ground truth locations
149 were used for disease recognition. A block diagram illustrating the different steps followed for
150 diseases quantification and mapping is shown in Figure (3).

151 Disease assessment was based on the following two methods:

1- Photo interpretation assessment (PIA): RGB photos collected from the ground truth plots were used in this analysis to assess crop disease coverage and incidence, defined by Chiarappa (1981) as the percentage cover of disease, and the number of individual infected plants in ratio to the healthy individuals, respectively. Images were overlaid with a 100-point grid at equal spacing as illustrated in Figure (4), adopting a similar approach to that proposed by Knight *et al.,* (2006). At the centre of each point, the object and health status were recorded and used to calculate the percent coverage of infection, or incidence of disease, an example is given in Table 2. This approach was adopted for both the yellow rust and fusarium assessment.

2- Infield visual assessment (IVA): Although visual assessment of crop diseases deemed to be subjective, it is the most common and adopted by partitions. IVA of both diseases at the ground truth plots were made at four levels, namely, the head (when present), at the flag leaves, at 2nd and 3rd leaves (mid canopy), and at the lower canopy. This was done in the field, at the time of the on-line scanning. Details on this method can be found in Part 1 of this study (Whetton *et al.,* 2017b). The assessment for fusarium head blight considered both early and later symptoms on heads, and were assessed as a percent of occurrence of infected ears. For yellow rust, quantitative assessments were recorded, for the percent of disease cover on the leaves.

2.5 Data analyses

2.5.1. Crop canopy spectral data pre-processing

The first step of spectra pre-processing included removing noisy wavelengths smaller than 400 nm and larger than 750 nm. Following the suggestion made in Whetton *et al.,* (2017a), the first and last 320 pixels were removed from each line scan. Noise removal was followed successively by reducing the number of variables by averaging three neighbouring wavelengths, maximum normalisation, first derivative and smoothing. All spectra pre-processing was carried out using Unscrambler 10 software (Camo Inc.; Oslo, Norway). Although pre-processing of spectral data includes techniques such as smoothing, if the process of cleaning the data is intensive due to noisy spectra it can lead to the loss of important spectral features, and thus impact on the success of analysis (Dasu & Johnson, 2003).

178 Therefore, a gentle smoothing of 2:2 was implemented during the first derivative and smoothing using
179 Savitzky–Golay algorithm. Detailed information about the spectra pre-processing steps can be found
180 in Martens & Naes (1989).

181 **2.5.2. Calibration models for prediction of yellow rust and fusarium head blight diseases**

182 For yellow rust analysis, the data from the five scans from the three wheat fields (Table 1) and the one
183 scan from the barley field were considered. However, for fusarium head blight the late captured data
184 of each field was used. This is because fusarium head blight occurs at a late crop growth stage, when
185 the ear emerges (51), and potential infection can occur when the crop is booting (43) by washing into
186 the sheath (Anand *et al.,* 2003).

187 Before running the PLSR analysis, the yellow rust dataset was divided into calibration (80%, e.g., 940
188 samples), non-mobile (spectra are captured at stationary state) validation (25%, e.g., 235 samples) and
189 on-line (spectra are captured on the move) validation (20%, e.g., 235 samples) sets. However, since at
190 each ground truth location 5 scans were collected, from which an average scan per location was
191 calculated. The final number of samples is reduced to 188 in the calibration set and 47 in each of the
192 non-mobile and on-line validation sets. Similar partitioning of samples was carried out for fusarium
193 samples, although smaller numbers of samples were available (124, 31 and 31 for calibration, non-
194 mobile validation and on-line validation, respectively). Statistical overview of samples used for PLSR
195 analyses for the assessment of yellow rust and fusarium head blight is shown in Table 3 and Table 4,
196 respectively, whereas statistics overview of samples used for on-line validation of PLSR models in
197 barley is shown in Table 5.

198 The pre-processed canopy spectral data was augmented with the estimated fungal diseases based on
199 PIA and IVA in one matrix. PLSR analyses with leave-one-out cross-validation was carried out on the
200 calibration datasets (75% of samples) using Unscrambler 10 software (Camo Inc.; Oslo, Norway).
201 PLSR. The input variables to PLSR were wavelengths (400-750 nm) and disease assessed as %
202 coverage, and the following four PLSR analyses were carried out:

1. Yellow rust based on IVA.
2. Yellow rust based on photo interpretation.
3. Fusarium head blight based on IVA.
4. Fusarium head blight based on photo interpretation.

Outliers were detected, and removed to a maximum of 5% of the total data. The wheat data was used to establish the PLSR calibration models, and underwent both cross-validation and independent validations (both non-mobile and on-line). No barley data was considered in the cross-validation, so that on-line disease predictions were carried out using the PLSR calibration models for wheat (Table 5). The performance of PLSR models were validated using the remaining 25% samples, which were not considered in the cross-validation stage. Validation was done using non-mobile collected spectra and the on-line collected data in the field by the mounted hyperspectral imager. For the on-line validation, predicted and assessed values were overlaid at the same or a very close position. However, the position of the on-line data did not always perfectly align to the ground truth spot position, due to the capture rate of the hyperspectral imager, and the accuracy of the DPGS system. Therefore, for validating the on-line predictions, a scanned area of 5 m^2 was considered, and the ground truth spot was located in the middle. This meant that for some ground truth points there were up to 3 on-line predicted values; the greatest match between measurement and prediction was used. This was done with ArcGIS 10 software (ESRI, California, USA).

The PLSR model performance was evaluated in cross-validation, non-mobile validation and on-line validation by means of R^2, root mean square error of prediction (RMSEP) and residual prediction deviation (RPD), which is the standard deviation of observations divided by RMSEP. In order to compare the performances of the different developed models we used a metric proposed by Whetton *et al.,* (2017b) for crop disease analysis. Details of different prediction performance categories are provided in Table 6.

2.5.3. Mapping of yellow rust and fusarium head blight diseases

Maps for the on-line predicted yellow rust and fusarium head blight were developed with ArcGIS 10 software (ESRI, California, USA). Kriging was used to develop maps from the data collected from the tramlines illustrated in Figure (2), assuming that the distance or direction between sample points reflects a spatial correlation that can be used to explain spatial variations. To distinguish these spatial variations, semi-variograms were developed in Rstudio (RStudio, Boston, MA) and then applied to the kriging by utilising the advanced parameters option in ArcGIS 10 software (ESRI, California, USA).

3. Results and Discussion

3.1. Crop canopy spectra analysis

Typical crop canopy spectra were recorded in the field for wheat (Figure 5) and barley (Figure 6), with similar spectral features to those reported by Whetton *et al.,* (2017b) under laboratory scanning conditions. However, the squared difference of 650 & 700 (nm) in field spectra is much larger than that in the laboratory spectra, which may indicate larger absorption in the 400-650 nm range by the darker canopy colour associated with larger intensity of chlorophyll in leaves. This large absorption (small reflectance) masks the significant band at 670 nm, associated with red colour band at 680 nm and linked to chlorophyll a (Hunt *et al.,* 2013).

Zhang and Zhang (2016) recommend the use of the spectral range of 470 to 800 nm sensitive to chlorophyll, to monitor crop diseases. Larger absorption (smaller relative reflectance) can be observed for a late stage captured spectra, as compared to early stage, which may be attributed to the increase of crop density and leaf area through the cropping season.

Furthermore, both on-line and non-mobile spectra captured late in the growing season were more similar to each other than the early spectra (Figure 5). This large similarity in spectra is a first indication of the good quality of the canopy spectra collected in this study under mobile condition.

Similarly, on-line and non-mobile spectra of barley canopy collected at anthesis growth stage show large similarity. Only slight differences in reflection can be observed at 520 – 550 nm and at 670 - 750 nm spectral ranges. Again the high similarity between the on-line and non-mobile spectra is a good indication of the hyperspectral system stability in providing high quality spectra to enable modelling yellow rust and fusarium head blight with desirable accuracy, to be evaluated in the following section.

3.2. Evaluation of model performance

Based on R^2 values in cross-validation (Table 7), it could be suggested that the performance of the wheat models is better for fusarium than for yellow rust predictions. The independent validation based on non-mobile collected spectra in the field indicates a similar trend to cross-validation (Table 7), where estimation of % coverage of yellow rust (RPD = 1.3 and 2.14 for PIA and IVA, respectively) is slightly less successful than for fusarium head blight (RPD = 1.4 and 2.31 for IVA and PIA, respectively). The PIA is worth performing for yellow rust prediction (RPD = 1.3), compared to IVA (RPD = 2.14), whereas the opposite is true for fusarium head blight (RPD = 2.31 for PIA and 1.4 for IVA). Therefore, the best non-mobile prediction performance of yellow rust obtained with IVA (RPD = 2.14) can be classified as a good prediction performance, whereas the best prediction performance for fusarium head blight obtained with PIA (RPD = 2.31) can also be classified as good prediction ability (Table 8). The implication of this result is that IVA should be adopted for yellow rust, and PIA for fusarium head blight under non-mobile measurement conditions.

It should discussed why IVA is better performing for yellow rust detection, while PIA for fusarium head blight. The reason is that the former consider infection of all parts on the canopy, while the

276 former based on RGB image might not capture yellow rust in the low canopy layers. This is the
277 reason why Zhao *et al.* (2016) recommended investigating the disease development for different leaf
278 layers. Fusarium head blight seems to be better captured in the RGB image than yellow rust as the
279 disease appears on heads that present at the top of the crop canopy; hence, fusarium disease is
280 unlikely to be obscured like yellow rust, allowing for an accurate count and representation to be made
281 with the PIA. The PIA also removes the potential of subjectivity between assessments. Due to yellow
282 rust being a foliar disease and there being overlapping in a canopy, the level of disease could be
283 hidden in an RGB image. Whilst it's arguable that the RGB photograph would be representing the
284 same area seen by the hyperspectral imager, the latter may pick up alterations in the crop's reflectance
285 due to yellow rust, which can be captured by the spectral data.

286 Huang *et al.* (2015) successfully assessed yellow rust in winter wheat, reporting a high R^2 value of
287 0.88, based on hyperspectral measurements of individual infected leaves, which is of limited use as
288 compared to canopy measurement adopted in the current work. Peteinatos *et al.* (2016) measured
289 spectral reflectance using two hand-held passive spectrometers and one fluorometer, and concluded
290 that early detection of yellow rust was possible. Adopting a data fusion approach of hyperspectral data
291 (450 – 900 nm) and fluorescence data (550 – 690 nm), Moshou *et al.* (2005), reported a high accuracy
292 (94.5 %) of detection for yellow rust in winter wheat. They needed two detection techniques to
293 achieve this accuracy, which makes the approach adopted rather expensive and complicated to use in
294 the field. Similar reliable results for quantitative identification of yellow rust in winter wheat have
295 been demonstrated by Krishna *et al.,* (2014), achieving high R^2 and RPD values of 0.90 of 3.8,
296 respectively. However, they have to include the entire visible and near infrared range (e.g., visible and
297 near infrared (VNIR) and short wavelength infrared (SWIR) of 350 to 2500 nm) to reach this
298 accuracy, whereas the current work achieved good (RPD = 2.14) prediction accuracy, based on a
299 relatively cost-effective hyperspectral camera, in the visible range only.

300 There is limited literature for fusarium head blight detection in the field, which may be attributed to
301 the difficult detection of symptoms appearing on ears. Polder *et al.,*(2005) reported successful

302 detection of fusarium head blight in single kernels, by using both spectroscopy and imaging.
303 Similarly, Delwiche and Kim (2000) successfully used a hyperspectral imager at 435 – 860 nm and
304 machine learning for fusarium head blight detection in wheat kernels. Bauriegel (2011) utilised a
305 hyperspectral imager, based on wavelength range intervals of 500–533 nm (green), 560–675 nm
306 (yellow), 682–733 nm (red) and 927–931 nm (red edge), to identify the percent coverage of fusarium
307 disease in ears, achieving average recognition accuracy of 67% and as high as 87%. Oerke and
308 Steiner (2010) utilised an infrared thermography for *in situ* detection of fusarium symptoms at a
309 canopy level, by detecting a significantly higher temperature in infected ears.

310 The non-mobile independent validation result for fusarium head blight in wheat (Table 7) is slightly
311 better (R^2 = 0.85, RMSEP = 0.39% and RPD = 2.31) than that of the on-line validation (R^2 = 0.82,
312 RMSEP = 0.63% and RPD = 2.27) (Table 8). This is expected as during on-line measurement
313 uncontrollable external conditions such as vibrations and variations in camera and light source heights
314 and angles negatively affect the measurement accuracy. However this is not the case for yellow rust in
315 wheat where a slightly (negligible) better prediction result is observed for the on-line measurement
316 (R^2 = 0.78, RMSEP = 6.13% and RPD = 2.19) compared to the non-mobile measurement (R^2 = 0.78,
317 RMSEP = 8.2% and RPD = 2.14). Results also show that the prediction of fusarium infection in wheat
318 (Table 8) is more accurate than in the barley, which can mainly be attributed to the fact that no
319 spectral data from barely were used in the cross-validation and that the PLSR prediction models
320 developed with wheat spectra only were used to predict these diseases in barely. Other reason might
321 be that wheat data being collected at a later growth stage (e.g., at Milk (70) in field 1 and 2 and at
322 anthesis (61) in field 4) than that for barley (anthesis (61), as shown in Table 1). Since fusarium head
323 blight infects the ear as opposed to the foliage, the impact of fusarium symptoms on spectra in less
324 pronounced in early growing stages (Rossi *et al.,* 2001; Xu, 2003). Indeed, fusarium models are only
325 applicable to late growing stages, when the ears have emerged.

326 For both non-mobile and on-line validations scenarios, yellow rust PLSR prediction models based on
327 IVA outperform the corresponding fusarium models (Table 7 and Table 8), whereas PIA is more

328 accurate for fusarium prediction. The PIA provides very poor on-line predictions of yellow rust, as
329 compared to those for fusarium in both barley and wheat fields. The IVA-based PLSR model
330 accuracy for on-line yellow rust prediction can be classified as good for wheat (RPD = 2.19, falling in
331 the category of 2 - 2.5 (Table 6) and as moderate for barley (RPD = 1.67 falling in the category of 1.5
332 - 2 (Table 6). The on-line prediction performance obtained with IVA-PLSR analysis of fusarium is
333 very poor (RPD = 0.47 and 0.75 for barley and wheat respectively). However, much better on-line
334 predictions of fusarium head blight is obtained with PIA, where the prediction accuracy is classified
335 as good for wheat (RPD = 2.27, falling in the category of 2 - 2.5 (Table 6) and moderate for barely
336 (RPD = 1.56, falling the category of 1.5 - 2 (Table 6). This results suggest that fusarium head blight
337 should be detected by PIA-PLSR models, whereas yellow rust by the IVA. This is true for both wheat
338 and barley. Similar to the non-mobile predictions, the on-line predictions in wheat were better than
339 those in the barley field, which is expected as models were created using data from wheat fields and
340 then applied to predict disease presence in the barley field to test robustness. Scatter plots of on-line
341 predicted versus reference assessed yellow rust and fusarium head blight are shown in Figure (7).

342 ## 3.3. Maps of yellow rust and fusarium head blight diseases

343 It is essential to explore the spatial variation of these crop diseases at high sampling resolution, which
344 is necessary for variable rate fungicide application (in case of yellow rust) or selective harvest (in case
345 of fusarium head blight). Furthermore, high sampling resolution data/maps can be combined with
346 weather data and incorporated into weather driven disease models to predict the potential spreading
347 pattern and enable early variable rate spraying even before the disease becomes visual.
348 The best models (e.g., PIA for fusarium head blight and IVA analysis for yellow rust) were selected
349 and used to develop corresponding maps in Figures (8) and (9), respectively. The best fit of the spatial
350 data for both disease in all fields are obtained with spherical semi-variograms, whose parameters are
351 shown in Table 9.
352 Examining the spatial distribution of fusarium head blight in the four studied fields, one can easily
353 observe that higher disease coverage appears at the edges, particularly for large area fields (e.g., fields

2, 3 and 4, shown in Figure (8). Similarly, in the first scans of yellow rust at early growing stage (Figure (9), high infection along the edges of the fields 1 and 3 is also recorded (no measurement was done for fields 2 and 4 due to a technical problem). It can be observed that fusarium spatial distribution in field 1 is significantly different than yellow rust, where high levels appear within the middle part of the field for fusarium (Figure 8) and field edges for yellow rust for both scanning occasions (Figure 9). The field edge pattern can be explained by the fact that both yellow rust and fusarium species can survive in soil and weeds occurring in the hedgerows and borders of a field, acting as a source of inoculum for the following cropping season (Imathiu *et al.,* 2013; Jenkinson and Parry, 1994; Champeil *et al.,* 2004). Initial infections of soil-borne pathogens, commonly result from infected plant residues left over from the previous year's harvest. Fusarium head blight fungi survive over winter on plant tissues and residues as mycelium (Sutton, 1982) and infected residues can produce ascospores and can infect the flag shoot (Oberti *et al.,* 2014), even after two years on the soil surface (Pereyra *et al.,* 2004).

It is important to point out here that the 7 ha sized field 4 (Figures. 9 & 10) can be split into two parts. This is in line with the different soil texture types observed for each part, with the north eastern (NE) half being of a heavier soil (clay loam), whilst the other southern west (SW) half being of a lighter soil (sandy clay loam). This split is also reflected on the moisture content map (Figure 10), where the average moisture content of side A is around 25% and side B is around 30 %. It's important to mention that the water content levels will vary in a short time period, but due to abiotic factors such as soil texture, elevation and soil depth the distribution pattern of high and low areas will remain steady. This field 4 was only scanned in one occasion at the milk (grain filling) stage on 1st July, 2015, which is quite late in the season. The largest yellow rust infection can be observed on the SW part of the field (Figure 9), whereas fusarium spatial distribution follows an opposite trend, where the highest infection is observed on NE part of the field (Figure 8). Due to the dry but warm conditions of 2015 spring, fusarium infection was low in general. It is of particular interest to mention that May according to the UK metrological office was particularly dry, and record breaking temperatures have

been reached later on in the season. This resulted in half of the field being under substantially more water stress (SW) than the other wetter half (NE), due to the difference in the soil texture type and its ability to retain soil moisture. Subsequently, this soil texture type and moisture retention differences between the two halves affect the crop canopy, and substantially impact the microclimate conditions of the crop. It was reported that a variation in soil texture can lead to variations in soil properties (Silver *et al*., 2000). For example, an increase in nitrogen will increase the duration and green area index of the canopy, which further affects the microclimate conditions (Stokes *et al.,* 1997; Sylvester-Bradley and Kindred, 2009). The underlying spatial distribution of moisture content in field 4 (Figure 10) confirms the NE part to have a larger moisture content than the SW part. This comes as a result of plants in the former part having denser, thicker and greener canopy (Part B in Figure 10), than plants in the dryer SW part (Part A in Figure 10). Whilst moisture content will vary quickly, the underlying spatial distribution pattern of water presence will remain similar through the season (Vachaud *et al.,* 1985). Local climate and weather conditions are considered the most influential factor regarding the distribution and severity of fungal infections in a crop stand. Under clear weather conditions in spring and summer, areas of the field with a lower crop density will warm up and cool down faster than those with dense canopies. Temperature in a wheat field's microclimate could have an inter-canopy variation of up to 7.5°C (Dammer, 2003), depending on crop canopy density and soil moisture content. Therefore, different soil texture type and subsequently moisture content encountered in this study have affected crop canopy density and humidity and crop health under the exceptional dry conditions in the spring of 2015, which led to the different disease spread pattern in among the two parts of the Field 4.

Literature demonstrates that epidemics of fungal diseases are strongly influenced by the local environment, persistence and adaption of the pathogen and the crops variety and physiological condition (Dammer, 2003). Therefore, variation in one of more of these will possibly affect disease distribution, which we believe to be the case in the 7 ha, field 4. Fusarium head blight is a sporadic disease, which is dependent on warm humid weather conditions, causing variability of disease

406 presence (Rossi *et al.,* 2001; Xu, 2003; Jelinek *et al.,* 1989). Furthermore, fusarium head blight is
407 primarily spread by water droplets (Broscious *et al.,* 1985; Sentelhas *et al.,* 1993). The requirement
408 for high humidity for fusarium head blight spread may explain why the NE part of field 4 is of higher
409 fusarium infection ranges than the dryer SW part. In the NE part the crop canopy is denser due to
410 heavier texture and larger MC which results in a higher humidity. However, the higher infection with
411 yellow rust in the dryer SW part of this field can be attributed to the fact that yellow rust spores are
412 predominantly dispersed by wind but require damp from rain or high humid conditions to infect the
413 crops leaves. The less dens canopy of the SW part, as compared to the NE part (Figure 10) allows for
414 better penetration of yellow rust spores by wind, hence increase infection rates in this part. This is an
415 interesting point to consider in plant protection against yellow rust and fusarium head blight, although
416 further investigations are necessary.

417 Due to the absence of high sampling resolution data on crop disease, the current farming practice is to
418 apply fungicide homogeneously, where low infected zones in the field are under dosed and highly
419 infected zones are overdosed. When data becomes available on the spatial distribution of these
420 diseases, variable rate fungicides can be applied using advanced variable rate technologies, and this is
421 expected to result in reducing the amount of fungicide applied and the associated environmental
422 impacts. Examining the spatial distribution of the on-line predicted fusarium head blight (Figure 8)
423 and yellow rust (Figure 9) maps, one can observe the high infection concentrated at the hedgerows
424 and borders of fields. This suggests the need for site specific application of fungicides that should
425 target these highly infected edge parts, and that application should take place at earlier growing
426 stages. This will prevent or at least reduce the possibility of diseases to expand towards the inner parts
427 of fields. Further work will need to use these maps for site specific fungicide applications, followed
428 by cost-benefit and life cycle analysis to evaluate the economic and environmental benefits as
429 compared to the traditional homogeneous applications adopted by majority of farmers today.
430 Developments into the use of hyperspectral imaging at field scale could be further investigated into
431 the use of unmanned aerial vehicles (UAVs), which would remove some limitations of ground

agricultural vehicles related to potential soil compaction, crop damage and low field-coverage efficiency.

4. Conclusions

This study explored the potential of a hyperspectral line imager (400-750 nm) for the on-line measurement and mapping of yellow rust and fusarium head blight in wheat and barley, to enable exploring the spatial variation of these crop diseases at high sampling resolution, which is necessary for variable rate fungicide application (in case of yellow rust) or selective harvest (in case of fusarium). The experiment was carried out in four fields, of which one field was cultivated with barley.

Yellow rust is more accurately measured using partial least squares regression (PLSR) prediction models developed with the traditional infield visual assessment (IVA) (RPD = 2.19, a performance classified as a good prediction capability in wheat and moderate prediction capability (RPD = 1.67) in barley. This is because IVA can capture yellow rust spots on low leaves, while the RGB photos considered for the photo interpretation assessment (PIA) fails to a given extent to do so. On the contrary, Fusarium on-line measurement was best performed based on PIA-PLSR models, where the accuracy was classified as good in wheat (RPD = 2.27) and moderate in barley (RPD = 1.56). This is believed to be due to fusarium symptoms appearing on ears, which can be satisfactorily captured by RGB images, than yellow rust attacking the foliage. Results achieved in this study showed that PLSR models developed for fusarium head blight and yellow rust in wheat, can be successfully applied to predict these diseases in barley with some reduction in accuracy.

The on-line developed maps confirmed the highest disease coverage to be at the field edges, which was attributed to the fact that these fungi diseases can survive in soil and weeds occurring in the hedgerows and borders of a field, acting as a source of inoculum for the following cropping season. The on-line disease map for one field, when compared to the moisture content map of the same field, revealed that soil texture and moisture content have considerable effect on disease spatial distribution,

457 due to their effect on canopy density and subsequently humidity, which in turn affect fusarium head
458 blight and yellow rust spatial pattern.

459 Further work is needed to evaluate the applicability of on-line maps of yellow rust for site specific
460 recommendations of fungicides and of fusarium head blight for selective harvest recommendations, as
461 the late in the cropping season measurement of fusarium head blight may not be useful for variable
462 rate fungicide applications.

463 Acknowledgement

464 We acknowledge the funding received for FarmFUSE project from the ICT-AGRI under the European
465 Commission's ERA-NET scheme under the 7th Framework Programme, and the UK Department of
466 Environment, Food and Rural Affairs (contract no: IF0208). The corresponding author
467 acknowledges the FWO funded Odysseus SiTeMan Project (Nr. G0F9216N).
468

469 References

470 Anand, A., Zhou, T., Trick, H.N., Gill, B.S., Bockus, W.W. and Muthukrishnan, S. (2003).
471 Greenhouse and field testing of transgenic wheat plants stably expressing genes for thaumatin-like
472 protein, chitinase and glucanase against Fusarium graminearum. *Journal of Experimental Botany*,
473 54(384), pp.1101-1111.

474 Bauriegel, E., Giebel, A., Geyer, M., Schmidt, U. and Herppich, W.B. (2011). Early detection of
475 Fusarium infection in wheat using hyper-spectral imaging.*Computers and Electronics in*
476 *Agriculture*, *75*(2), pp. 304-312.

477 Bock, C.H., Poole, G.H., Parker, P.E. and Gottwald, T.R. (2010). Plant disease severity estimated
478 visually, by digital photography and image analysis, and by hyperspectral imaging. *Critical Reviews*
479 *in Plant Sciences*, 29(2), pp. 59-107

480 Bravo, C., Moshou, D., West, J., McCartney, A., & Ramon, H. (2003). Early disease detection in
481 wheat fields using spectral reflectance. *Biosystems Engineering*, 84(2), pp. 137-145.
482 Bravo, C., Moshou, D., West, J., McCartney, A. and Ramon, H., 2003. Early disease detection in
483 wheat fields using spectral reflectance. *Biosystems Engineering*, *84*(2), pp.137-145

484 Brennan, J.M., Egan, D., Cooke, B.M, Doohan, F.M. (2005). Effect of temperature on head blight of
485 wheat caused by Fusarium culmorum and F. graminearum. *Plant Pathology*, 54, 156.

Broscious, S.C., Frank, J.A., & Frederick, J.R. (1985). Influence of winter wheat management practices on the severity of powdery mildew and Septoria blotch in Pennsylvania. *Phytopathology*, pp. 75, pp. 538–542.

Champeil, A., Dore, T. and Fourbet, J.F. (2004). Fusarium head blight: epidemiological origin of the effects of cultural practices on head blight attacks and the production of mycotoxins by Fusarium in wheat grains. *Plant science*, 166(6), pp. 1389-1415.

Chiarappa L., ed. (1981). Crop Loss Assessment Methods — Supplement 3. Wallingford; CAB International.

Dammer, K.-H. (2003). In: Investigations into the dynamic of climatic parameters and infections with fungi diseases in heterogeneous cereal stands (p. 23). Potsdam, Germany: Jahresbericht des ATB.

Dasu, T., & Johnson, T. (2003). Exploratory data mining and data cleaning (Vol. 479). John Wiley & Sons.

Delwiche, S.R. and Kim, M.S., 2000, December. Hyperspectral imaging for detection of scab in wheat. In *Environmental and Industrial Sensing* (pp. 13-20). International Society for Optics and Photonics

Desjardin, A.E. (2006). Fusarium mycotoxins. Chemistry, Genetics, and Biology. APS Press, St. Paul, MN.

Gómez-Casero, M.T., Castillejo-González, I., García-Ferrer, A., Peña-Barragán, J.M., Jurado-Expósito, M., García-Torres, L. and López-Granados, F. (2010). Spectral discrimination of wild oat and canary grass in wheat fields for less herbicide application. *Agronomy for Sustainable Development*, 30(3), pp. 689-699.

Hahn, F., (2009). Actual pathogen detection: Sensors and algorithms—a review. Algorithms 2, 301–338.

Huang, L.S., Ju, S.C., Zhao, J.L., Zhang, D.Y., Teng, L. and Yang, F. (2015). Hyperspectral Measurements for Estimating Vertical Infection of Yellow Rust on Winter Wheat Plant. *International Journal of Agriculture & Biology*, 17(6), pp. 1234-1241.

Hunt, E.R., Doraiswamy, P.C., McMurtrey, J.E., Daughtry, C.S., Perry, E.M. and Akhmedov, B., 2013. A visible band index for remote sensing leaf chlorophyll content at the canopy scale. *International Journal of Applied Earth Observation and Geoinformation*, *21*, pp.103-112

Imathiu, S.M., Edwards, S.G., Ray, R.V. and Back, M.A. (2013). Fusarium langsethiae–a HT-2 and T-2 Toxins Producer that Needs More Attention. *Journal of Phytopathology*, 161(1), pp.1-10

Jelinek CF, Pohland AE, Wood GE. (1989) Worldwide occurrence of mycotoxins in foods and feeds-An update. *J AOAC Int*, 72, pp. 223–230.

Jenkinson, P. and Parry, D.W. (1994). Splash dispersal of conidia of Fusarium culmorum and Fusarium avenaceum. *Mycological Research*, 98(5), pp.506-510.

Knight, J.F., Lunetta, R.S., Ediriwickrema, J. and Khorram, S. (2006). Regional scale land cover characterization using MODIS-NDVI 250 m multi-temporal imagery: A phenology-based approach. *GIScience & Remote Sensing*, 43(1), pp.1-23.

524 Krishna, G., Sahoo, R.N., Pargal, S., Gupta, V.K., Sinha, P., Bhagat, S., Saharan, M.S., Singh, R. and
525 Chattopadhyay, C., 2014. Assessing wheat yellow rust disease through hyperspectral remote
526 sensing. *The International Archives of Photogrammetry, Remote Sensing and Spatial Information*
527 *Sciences*, 40(8), p. 1413.

528 Kuang, B. & Mouazen, A.M., (2013). Non-biased prediction of soil organic carbon and total nitrogen
529 with vis–NIR spectroscopy, as affected by soil moisture content and texture. *Biosystems*
530 *engineering*, 114(3), pp. 249-258.

531 Leslie, J.F., Summerell, B.A. (2006). The Fusarium Laboratory Manual. Blackwell Publishing, Ames,
532 IA

533 Magan, N., Hope, R., Colleate, A., & Baxter, E. S. (2002). Relationship Between Growth and
534 Mycotoxin Production by Fusarium species, Biocides and Environment. *European Journal of Plant*
535 *Pathology*, 108(7), pp. 685-690.

536 Martens, H. and Naes, T. (1989). Assessment, validation and choice of calibration
537 method. *Multivariate calibration*, pp. 237-266

538 Milus, E.A., Kristensen, K., & Hovmøller, M.S. (2009). Evidence for increased aggressiveness in a
539 recent widespread strain of Puccinia striiformis f. sp. tritici causing stripe rust of
540 wheat. Phytopathology, 99(1), 89-94.

541 Moshou, D., Bravo, C.,West, J.,Wahlen, S., McCartney, A., Ramon, H. (2004). Automatic detection
542 of 'yellow rust' in wheat using reflectance measurements and neural networks. Computers and
543 Electronics in Agriculture 44 (3), 173–188.

544 Mouazen, A.M., Anthonis, J., & Ramon, H., (2005). An automatic depth control system for online
545 measurement of spatial variation in soil compaction, Part 4: improvement of compaction maps by
546 using a proportional integrative derivative depth controller. *Biosystems Engineering*, 90(4), pp. 409-
547 418.

548 Moshou, D., Bravo, C., Oberti, R., West, J., Bodria, L., McCartney, A. and Ramon, H. (2005). Plant
549 disease detection based on data fusion of hyper-spectral and multi-spectral fluorescence imaging
550 using Kohonen maps. *Real-Time Imaging*, 11(2), pp.75-83.

551 Mouazen, A.M. (2006). Soil Survey Device. International publication published under the patent
552 cooperation treaty (PCT). World Intellectual Property Organization, International Bureau.
553 International Publication Number: WO2006/015463; PCT/BE2005/000129; IPC: G01N21/00;
554 G01N21/00.

555 Oberti, R., Marchi, M., Tirelli, P., Calcante, A., Iriti, M., & Borghese, A.N. (2014). Automatic
556 detection of powdery mildew on grapevine leaves by image analysis: Optimal view-angle range to
557 increase the sensitivity. *Computers and Electronics in Agriculture*, 104, 1-8.

558 Oerke, E.C. and Steiner, U., 2010. Potential of digital thermography for disease control. In *Precision*
559 *Crop Protection-the Challenge and Use of Heterogeneity* (pp. 167-182). Springer Netherlands

560 Peteinatos, G.G., Korsaeth, A., Berge, T.W. and Gerhards, R. (2016). Using Optical Sensors to
561 Identify Water Deprivation, Nitrogen Shortage, Weed Presence and Fungal Infection in
562 Wheat. *Agriculture*, *6*(2), p.24.

563 Polder, G., Van Der Heijden, G.W.A.M., Waalwijk, C. and Young, I.T., 2005. Detection of Fusarium
564 in single wheat kernels using spectral imaging. *Seed Science and Technology*, *33*(3), pp.655-668.

565 Roggo, Y., Duponchel, L., & Huvenne, J.P. (2003). Comparison of supervised pattern recognition
566 methods with McNemar's statistical test: application to qualitative analysis of sugar beet by near-
567 infrared spectroscopy. *Analytica Chimica Acta*, 477(2), pp. 187–200.

568 Rossi V, Ravanetti A, Pattori E, Giosue S. (2001) Influence of temperature and humidity on the
569 infection of wheat spikes by some fungi causing fusarium head blight. *J Plant Pathol*, 83, pp. 189–
570198.

571 Rotter, B.A., Prelusky, D.B., Pestka, J.J. (1996). Toxicology of deoxynivalenol (vomitoxin). *Journal*
572 *of Toxicology and Environmental Health,* 48, pp. 1–34.

573 Saeys, W.; Mouazen, A.M.; Ramon, H. (2005). Potential for onsite and online analysis of pig manure
574 using visible and near infrared reflectance spectroscopy. *Biosystems Engineering*, 91(4), pp. 393-402.

575 Schmale, D.G., III, & Bergstrom, G.C. (2003). Fusarium head blightin wheat. The Plant Health
576Instructor. http://dx.doi.org/10.1094/PHI-I-2003-0612-01.

577 Sentelhas, P.C., Pedro, M.J., & Felicio, J.C. (1993). Effects of different conditions of irrigation and
578 crop density on microclimate and occurrence of spot blotch and powdery mildew. *Bragantia*, 52, pp.
57945–52.

580 Silver, W.L., Neff, J., McGroddy, M., Veldkamp, E., Keller, M. and Cosme, R., 2000. Effects of soil
581 texture on belowground carbon and nutrient storage in a lowland Amazonian forest
582 ecosystem. *Ecosystems*, 3(2), pp. 193-209.

583 Stokes D.T., Scott R.K., Sylvester-Bradley R. et al. (1997). An Integrated Approach to Nitrogen
584 Nutrition for Wheat. London, UK: Home-Grown Cereals Authority: Project Report No. 159.

585 Sutton, J.C. (1982). Epidemiology of wheat head blight and maize ear rot caused by Fusarium
586 graminearum. *Canadian Journal of Plant Pathology*, 4, 195.

587 Sylvester-Bradley R., Kindred D. (2009). Analysing nitrogen responses of cereals to prioritise routes
588 to the improvement of nitrogen use efficiency. *Journal of Experimental Botany*, 60, pp. 1939–51.

589 Vachaud, G., Passerat de Silans, A., Balabanis, P. and Vauclin, M., 1985. Temporal stability of
590 spatially measured soil water probability density function. *Soil Science Society of America*
591*Journal* , *49*(4), pp. 822-828

592 West, J.S., Bravo, C., Oberti, R., Lemaire, D., Moshou, D. and McCartney, H.A. (2003). The potential
593 of optical canopy measurement for targeted control of field crop diseases. *Annu. Rev. Phytopathol*, 41,
594pp. 593-614.

595 Whetton R.L., Waine T.W. & Mouazen, A.M. (2017a). Optimising configuration of a hyperspectral
596 imager for on-line field measurement of wheat canopy. *Biosystems Engineering*, 155, pp. 84-95.

597 Whetton, R.L., Waine, T.W. & Mouazen, A.M. (2017b). Hyperspectral measurements of yellow rust
598 and fusarium in cereal crops: Part 1: Laboratory study, *Biosystems Engineering,* 166, pp. 101-115.

599 Wu, D., Feng, L., Zhang, C., & He, Y., (2008). Early detection of Botrytis cinerea on eggplant leaves
600 based on visible and near-infrared spectroscopy. *Transactions of the ASABE* 51 (3), pp. 1133–1139.

Xu X.M. (2003) Effects of environmental conditions on the development of fusarium ear blight. *Eur J Plant Pathol,* 109. pp. 683–689.

Zadoks, J.C., Chang, T.T., & Konzak C.F. (1974). A decimal code for the growth stages of cereals. *Weed Research,* 14(6), pp. 415–421.

Zhang, H., Hu, H. and Zhang, H. (2016). Monitoring Methods of Crop Diseases and Pests Based on Hyperspectral Technology. *International Journal of Simulation--Systems, Science & Technology*, 17(11), pp.2.1-2.5.

Zhao, J., Zhang, D., Huang, L., Zhang, Q., Liu, W. & Yang, H. (2016).. Vertical features of yellow rust infestation on winter wheat using hyperspectral imaging measurements. In *Agro-Geoinformatics (Agro-Geoinformatics), 2016 Fifth International Conference on* (pp. 1-4). IEEE.

Zhou, B., Elazab, A., Bort, J., Vergara, O., Serret, M.D. & Araus, J.L. (2015). Low-cost assessment of wheat resistance to yellow rust through conventional RGB images. *Computers and Electronics in Agriculture*, 116, pp. 20-29.

635 **Figure captions**

636 **Figure 1:** Hyperspectral imagery system mounted on a metal frame attached to the side of a tractor,
637 ready for on-line canopy measurement.

638 **Figure 2:** On-line hyperspectral measurement lines and position of ground truth plots, collected at
639 five samples per ha, in the four fields**.** Fields 1 and 4 were validated at the same locations at two time
640 intervals.

641 **Figure 3:** A block diagram illustrating the different steps followed for diseases quantification and
642 mapping.

643 **Figure 4:** Example of photo interpretation based assessment of % coverage of yellow rust and
644 fusarium head blight based on a 100-point grid.

645 **Figure 5:** Spectra of wheat canopy collected at early (booting) and late (milk) growth stages,
646 comparing on-line and non-mobile (off-line ground truth) spectra as: (-) late non-mobile (---) early
647 non-mobile (…) early on-line, and (_ _) late on-line.

648 **Figure 6:** Spectra of barley canopy collected at anthesis growth stage, comparing between on-line (--)
649 and non-mobile (-) spectra

650 **Figure 7:** Scatter plots of on-line measured versus predicted % coverage of yellow rust in wheat
651 infield with visual assessment (IVA)-based partial least squares regression (PLSR) model (a), IVA-
652 PLSR prediction of yellow rust in barley (b), photo interpretation assessment (PIA)-based PLSR
653 model prediction of fusarium head blight in wheat (c) and PIA-PLSR prediction fusarium head blight
654 in barley (d).

655 **Figure 8:** On-line measured fusarium maps in the four experimental fields; field 1 with wheat (a) (4
656 ha anthesis), field 2 with barley (b) (10 ha anthesis), field 3 with wheat (c) (12 ha Milk), and field 4
657 with wheat (d) (7 ha Milk).

Figure 9: On-line measured yellow rust maps in the four experimental fields: (a and b) refer to maps of early stage scans in field 1 with wheat (4 ha booting) and field 3 with wheat (12 ha booting), respectively. Maps of late stage scans are shown by (c) for field 3 with wheat (12 ha Milk), (d) for field 4 with wheat (7 ha Milk) (e) for field 1 with wheat (4 ha anthesis) and (f) field 2 with barley (10 ha anthesis).

Figure 10: Soil moisture content map measured with the on-line visible and near infrared spectroscopy sensor (Mouazen, 2006) and RGB images of crop in field 4.

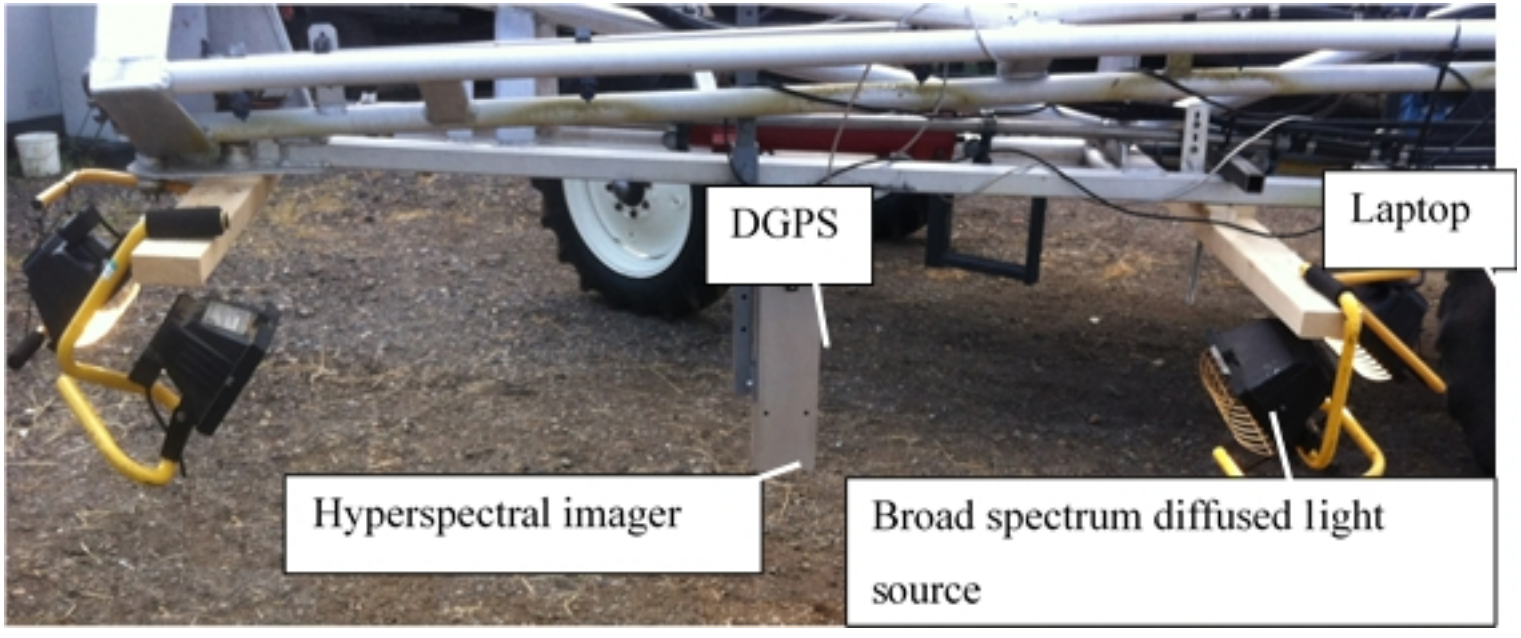
DGPS
Laptop
Hyperspectral imager
Broad spectrum diffused light source

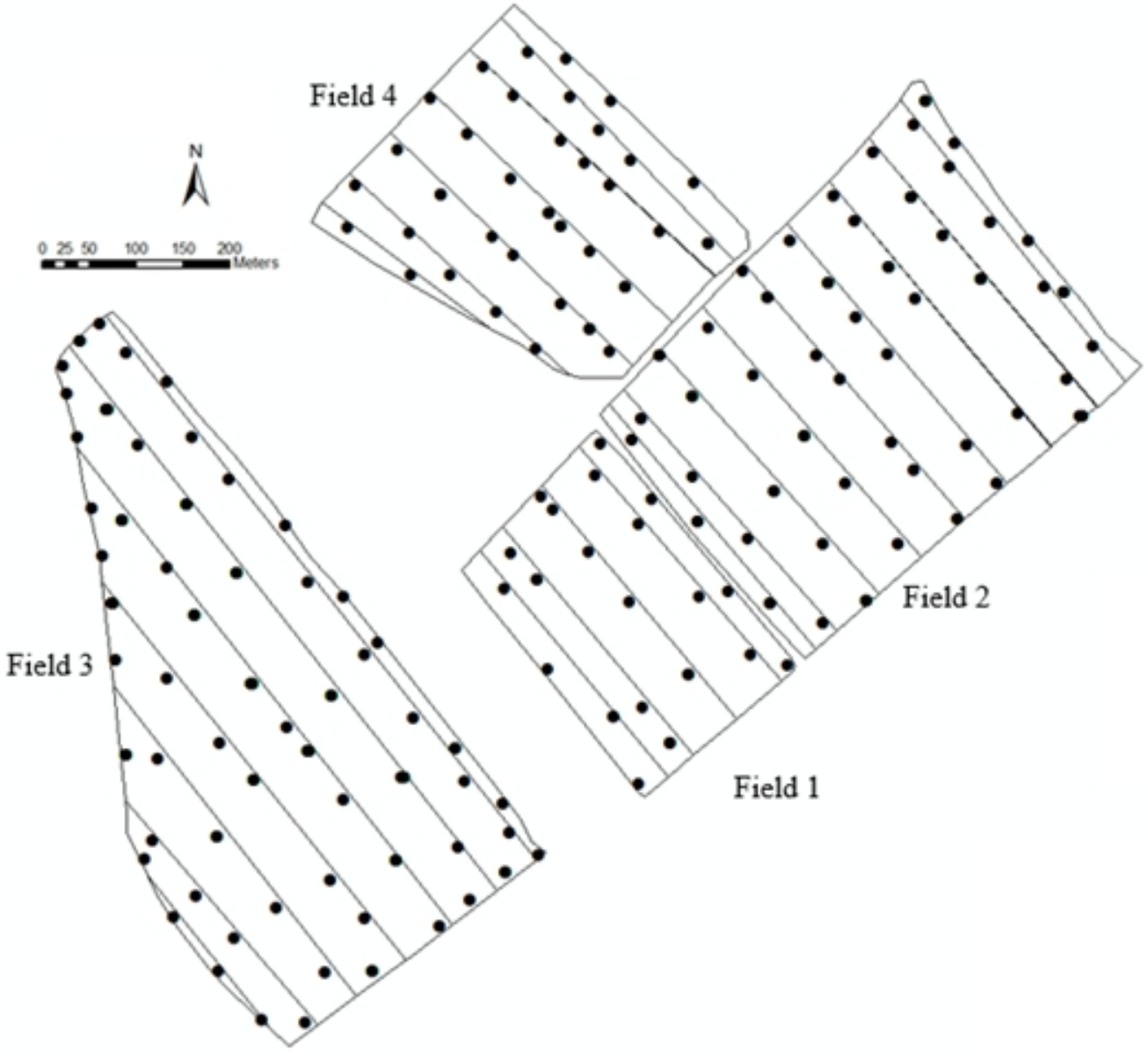
Field 4
N
0 25 50 100 150 200
Meters
Field 2
Field 3
Field 1

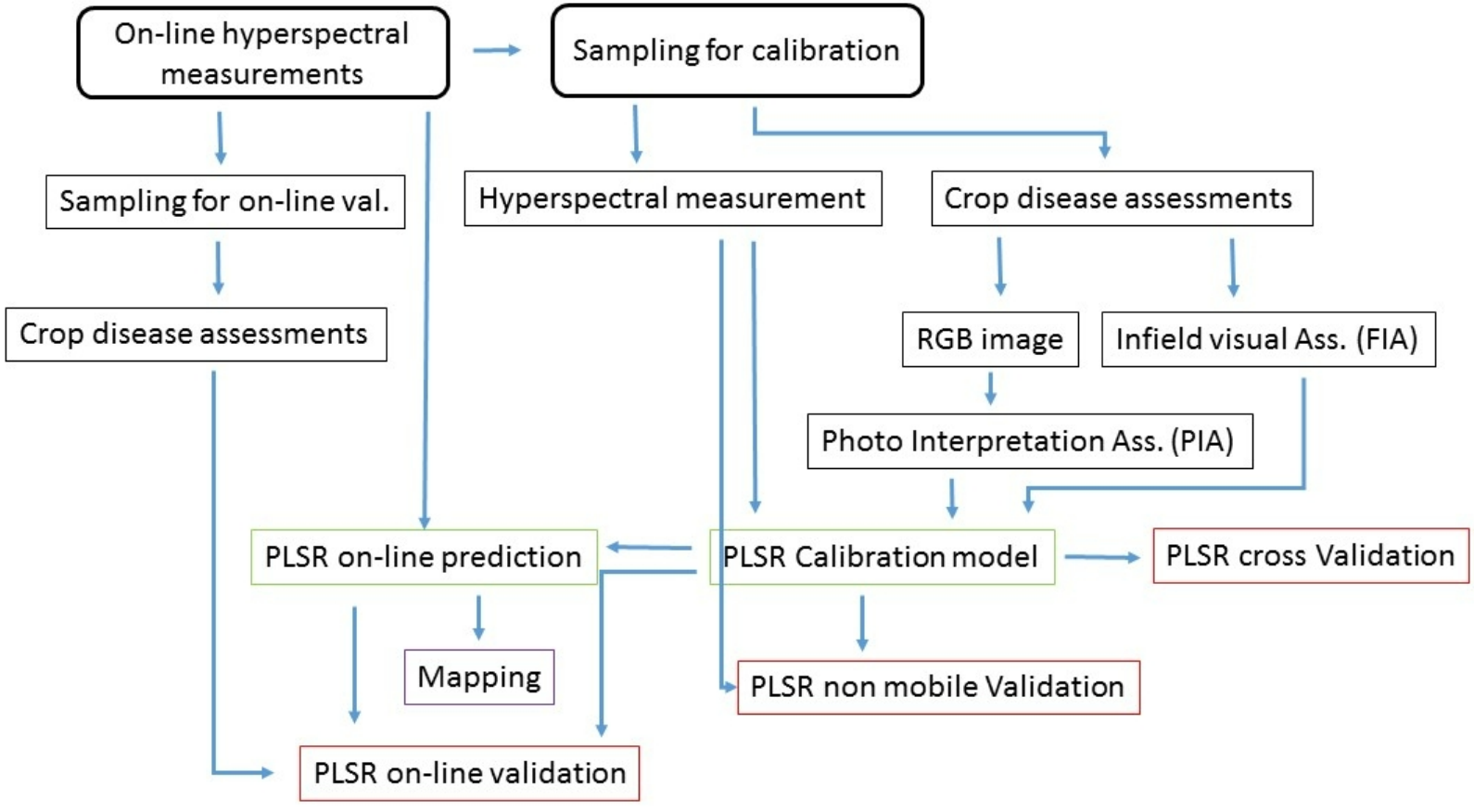
On-line hyperspectral measurements
Sampling for calibration
Sampling for on-line val.
Hyperspectral measurement
Crop disease assessments
Crop disease assessments
RGB image
Infield visual Ass. (FIA)
Photo Interpretation Ass. (PIA)
PLSR on-line prediction
PLSR Calibration model
PLSR cross Validation
Mapping
PLSR non mobile Validation
PLSR on-line validation

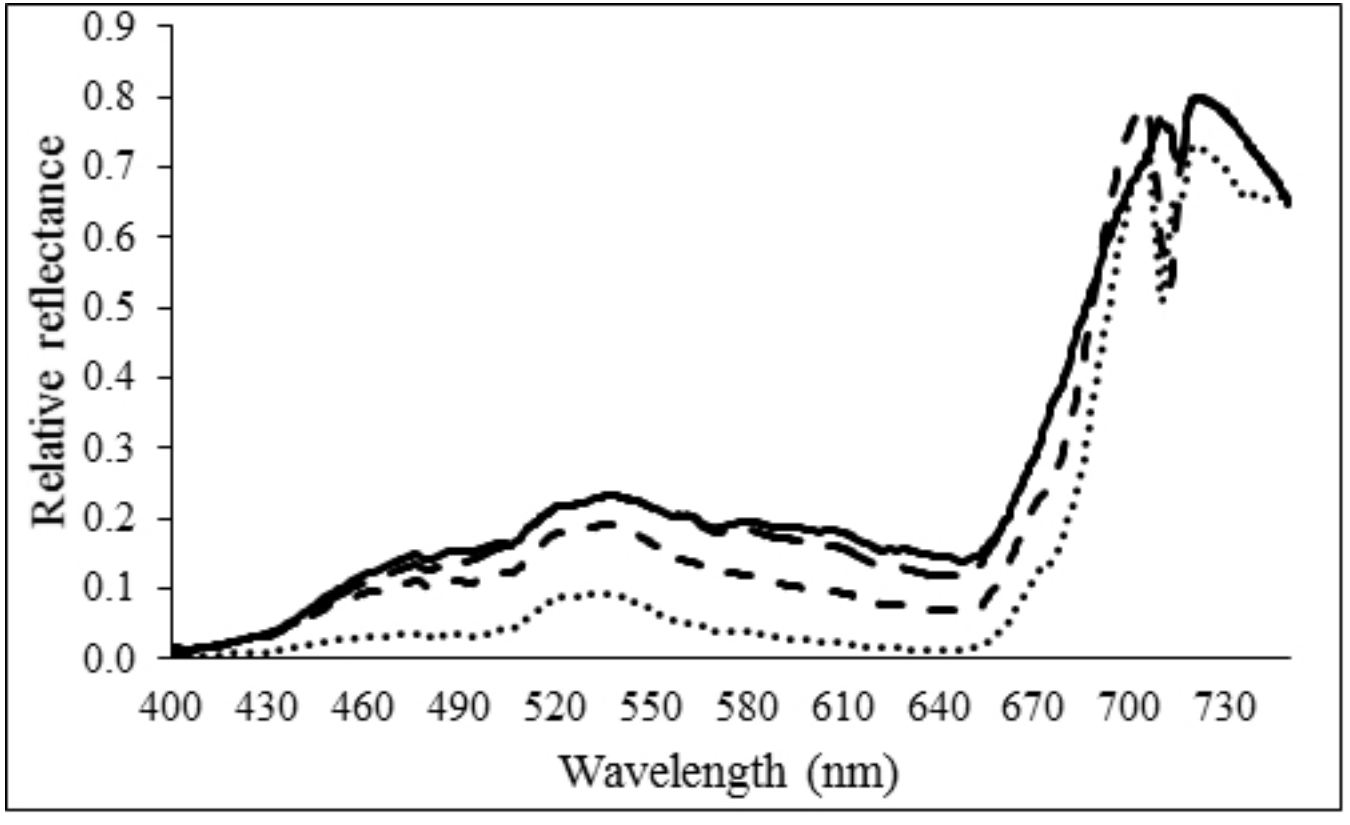
0.9
0.8
0.7
0.6
0.5
0.4
0.3
0.2
0.1
0.0
Relative reflectance
400
430
460
490
520
550
580
610
640
670
700
730
Wavelength (nm)

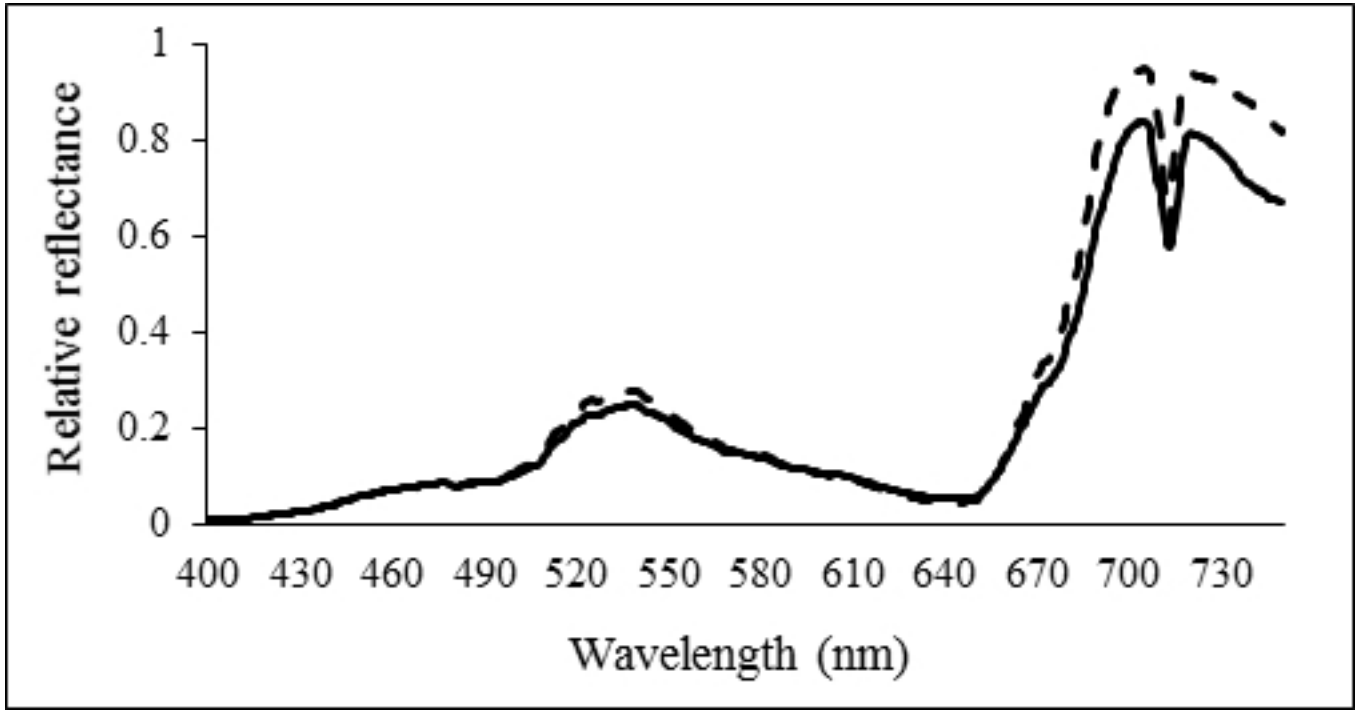
Relative reflectance
1
0.8
0.6
0.4
0.2
0
400 430 460 490 520 550 580 610 640 670 700 730
Wavelength (nm)

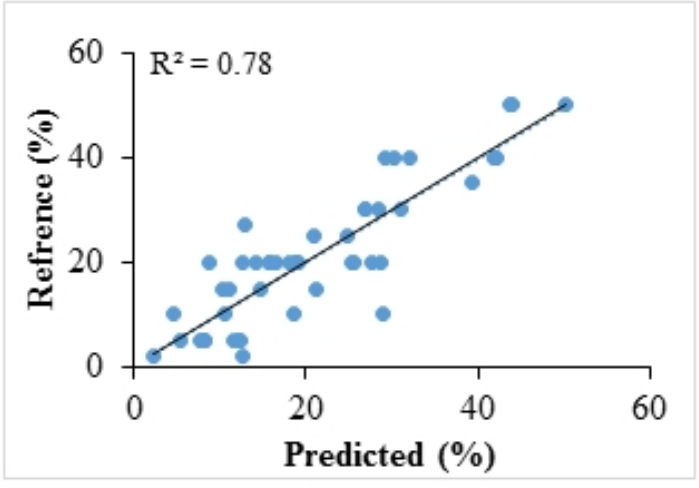
R² = 0.78
Refrence (%)
Predicted (%)
0
20
40
60

A

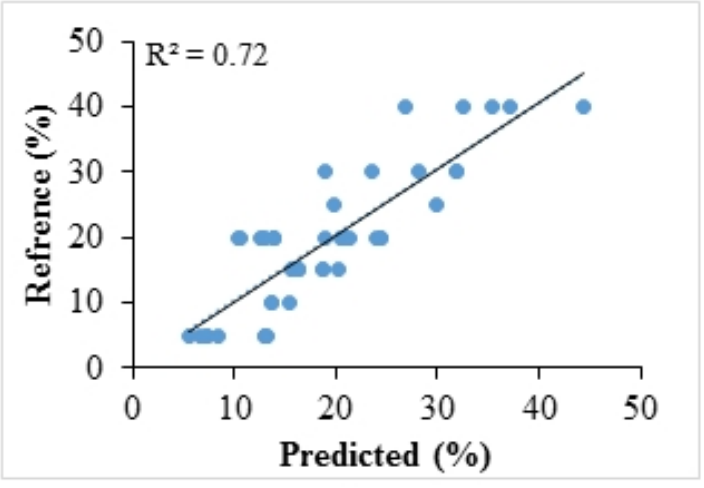
R² = 0.72
Refrence (%)
Predicted (%)
0
10
20
30
40
50

B

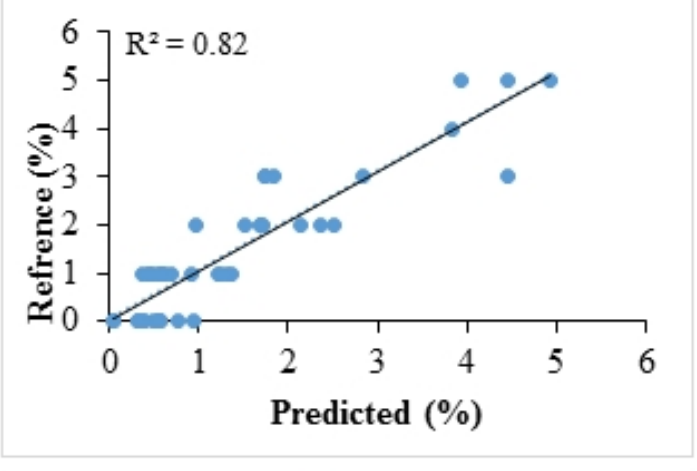
R² = 0.82
Refrence (%)
Predicted (%)
0
1
2
3
4
5
6

C

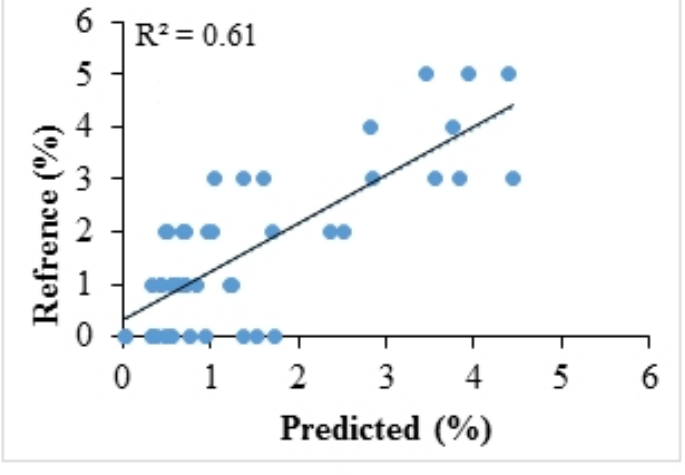
R² = 0.61
Refrence (%)
Predicted (%)
0
1
2
3
4
5
6

D

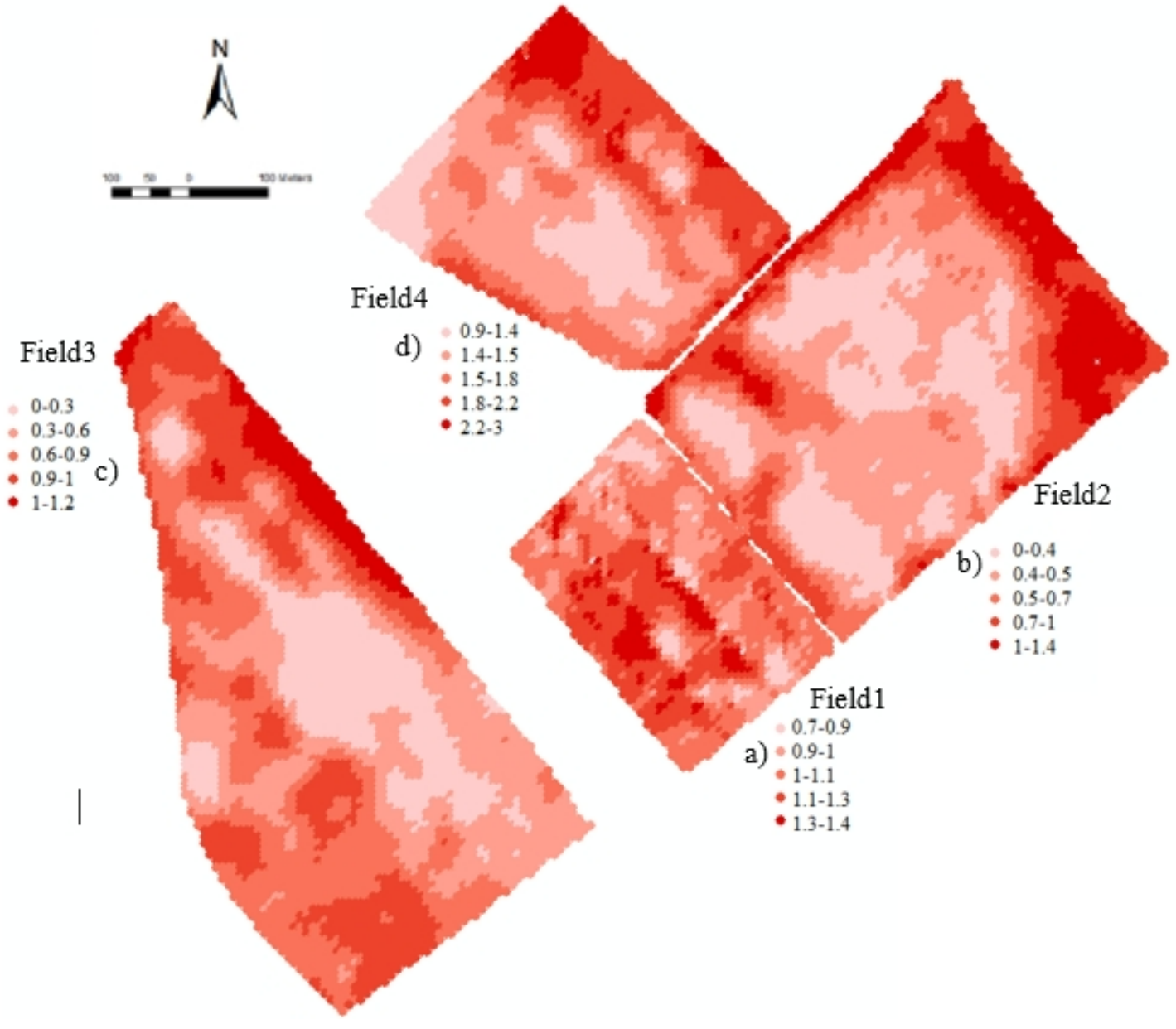
N
100 50 0 100 Meters
Field4
d)
0.9-1.4
1.4-1.5
1.5-1.8
1.8-2.2
2.2-3
Field3
0-0.3
0.3-0.6
0.6-0.9
0.9-1
1-1.2
c)
Field2
b)
0-0.4
0.4-0.5
0.5-0.7
0.7-1
1-1.4
Field1
a)
0.7-0.9
0.9-1
1-1.1
1.1-1.3
1.3-1.4

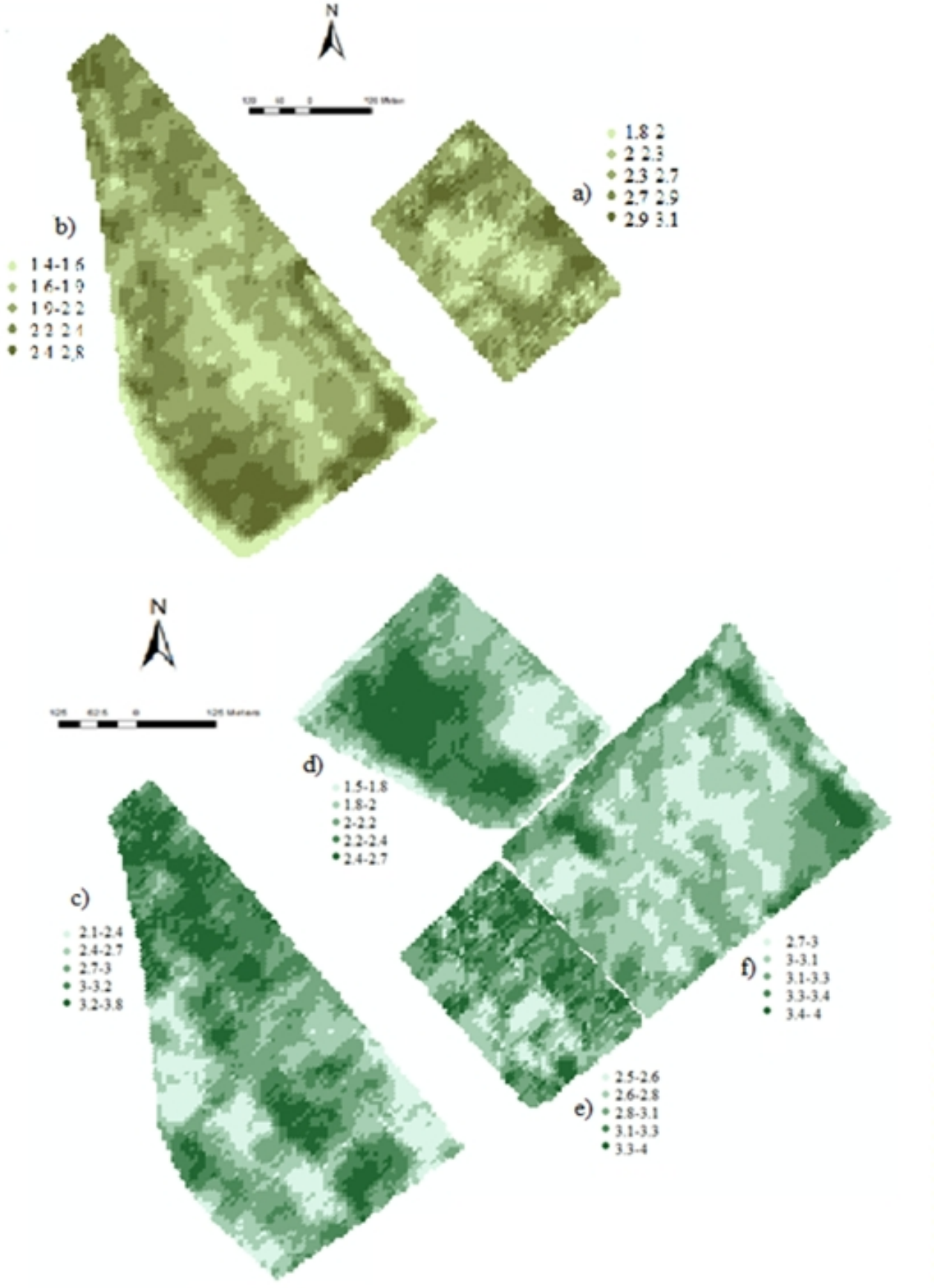
N
a)
1.8 2
2 2.3
2.3 2.7
2.7 2.9
2.9 3.1
b)
1.4-1.6
1.6-1.9
1.9-2.2
2.2 2.4
2.4 2.8
N
d)
1.5-1.8
1.8-2
2-2.2
2.2-2.4
2.4-2.7
c)
2.1-2.4
2.4-2.7
2.7-3
3-3.2
3.2-3.8
f)
2.7-3
3-3.1
3.1-3.3
3.3-3.4
3.4-4
e)
2.5-2.6
2.6-2.8
2.8-3.1
3.1-3.3
3.3-4

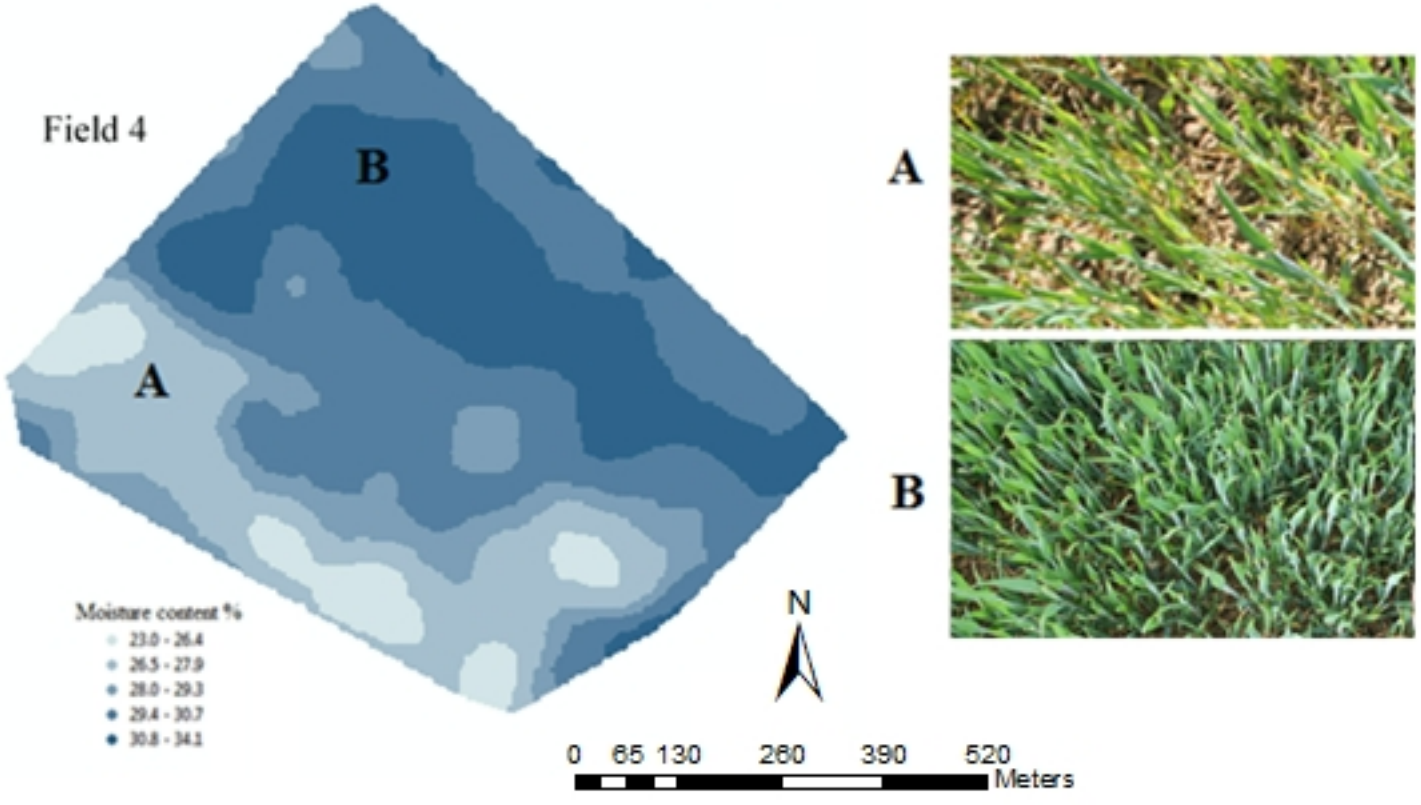
Field 4
B
A
Moisture content %
23.0 - 26.4
26.5 - 27.9
28.0 - 29.3
29.4 - 30.7
30.8 - 34.1
N
0 65 130 260 390 520
Meters
A
B

Table 1: Experimental fields**,** scanning time and growth stage identified according to the Zadok's scale (Zadoks *et al.,* 1974). The soil type is presented for northern (N), southern (S) or eastern (E) and western (W) parts of a field.

Field Number	**Field area (ha)**	**Crop**	**Soil type**	**Date of scanning**	**Crop stage**
1	4	Winter wheat	Sandy clay	04/06/2015 30/06/2015	Booting (43) Anthesis (61)
2	10	Winter barley	N: Clay S: Sandy clay	27/05/2015	Anthesis (61)
3	12	Winter wheat	E: Clay W: sandy clay loam	22/05/2015 01/07/2015	Booting (43) Milk (70)
4	7	Winter wheat	E: clay loam W: sandy clay loam	01/07/2015	Milk (70)

Table 2: An example for the calculation of the % coverage of yellow rust and fusarium based on a 100-point grid overlaid on an RGB image.

Object in centroid	**Occurrence**	**Disease coverage (%)**
Healthy leaf	30	15 for yellow rust
Yellow rust leaf	15	
Healthy ear	20	3 for fusarium
Fusarium ear	3	
Stem	7	NA
Other (e.g., bare soil, senesced leaf)	25	NA

Table 3: Statistical overview of samples used for the partial least squares regression (PLSR) analyses for the assessment of yellow rust in wheat.

	Infield visual assessment (IVA) (%)			**Photo interpretation assessment (PIA) (%)**		
	Cross-val.	Non-mobile	On-line	Cross-val.	Non-mobile	On-line
Nr	188	47	47	188	47	47
Max	90	65	50	60	65	50
Min	0	2	2	0	2	2
Mean	15	20	20	7	10	10
SD	17	18	13.4	14	12	16

SD is standard deviation

Table 4: Statistical overview of samples used for the partial least squares regression (PLSR) analyses for the assessment of fusarium in wheat.

	Infield visual assessments (IVA) (%)			**Photo interpretation assessment (PIA) (%)**		
	Cross-val	Non-mobile	On-line	Cross-val	Non-mobile	On-line
Nr	124	31	31	124	31	31
Max	5	3	5	3	2	3
Min	0	0	0	0	0	0
Mean	0.9	0.5	0.6	0.7	0.5	0.6
SD	1.7	0.9	1.4	1.3	0.7	1.4

SD is standard deviation

Table 5: Statistical overview of samples used for on-line validation of yellow rust and fusarium in barley.

	Fusarium		Yellow rust	
	Infield visual assessments (IVA) (%)	**Photo interpretation assessment (PIA) (%)**	**Infield visual assessments (IVA) (%)**	**Photo interpretation assessment (PIA) (%)**
Nr	50	50	50	50
Max	5	3	40	58
Min	2	1	0	3
Mean	2.6	1.9	5	20
SD	1.3	1.5	9	13

SD is standard deviation

Table 6: Classes of the ratio of prediction deviation (RPD) and their suitability for predicting yellow rust and fusarium in cereal crops, proposed by Whetton *et al.,* (2017b).

RPD range	Class and prediction capability
< 1	Poor model predictions - not useful.
1-1.5	Possibility to discriminate between low and high values
1.5-2.0	Moderate prediction capability
2.0-2.5	Good prediction capability
2.5-3.0	Very good prediction capability
>3.0	Excellent prediction capability

Table 7: Summary of prediction performance of % coverage of yellow rust and fusarium in wheat in cross-validation and non-mobile independent validation. Models were developed with the five on-line scanning occasions in three wheat fields.

		Fusarium		**Yellow rust**	
		Infield visual assessment (IVA)	Photo interpretation assessment (PIA)	Infield visual assessment (IVA)	Photo interpretation assessment (PIA)
Cross validation	R^2	0.86	**0.87**	**0.79**	0.74
	RMSCV (%)	0.51	**0.25**	**8.19**	8.21
Non-mobile validation	R^2	0.71	**0.85**	**0.78**	0.005
	RMSEP (%)	0.5	**0.39**	**8.2**	9.2
	RPD	1.4	**2.31**	**2.14**	1.3

RMSECV is root mean square error of cross validation; RMSEP is root mean square error of prediction; RPD is ratio of prediction deviation = standard deviation / RMSEP

Table 8: Summary of prediction performance of % coverage of yellow rust and fusarium in on–line validation using spectral data collected from three wheat fields and one barley field.

		Fusarium		**Yellow rust**	
		Infield visual assessment (IVA)	Photo interpretation assessment (PIA)	Infield visual assessment (IVA)	Photo interpretation assessment (PIA)
Wheat	R^2	0.04	**0.82**	**0.78**	0.06
	RMSEP (%)	1.93	**0.63**	**6.13**	22.88
	RPD	0.75	**2.27**	**2.19**	0.7
Barley	R^2	0.09	**0.61**	**0.72**	0.045
	RMSEP (%)	2.69	**0.93**	**5.39**	26.59
	RPD	0.47	**1.56**	**1.67**	0.49

RMSEP is root mean square error of prediction; RPD is ratio of prediction deviation = standard deviation / RMSEP

Table 9: Semi-variogram model parameters of each mapped disease in the four fields. The best fit was achieved with spherical models.

		Semi-variogram parameters				
		Nugget	**Range**	**Sill**	**Proportion**	**Sum of square error**
Fusarium	Field 1	0.12	86.39	0.71	5.51	2.95
	Field 2	0.37	99.46	0.83	1.70	1.41
	Field 3	0.11	97.02	0.89	8.02	3.32
	Field 4	0.04	75.62	0.77	18.98	0.00
yellow rust early	Field 1	0.001	77.75	0.002	1.001	3.383
	Field 2	0.001	68.1	0.003	2.002	8.029
	Field 3	0.0001	78.34	0.001	9.0009	2.56
	Field 4	0.02	76.63	0.043	1.173	0.0021
yellow rust late	Field 1	0.01	77.75	0.022	1.212	2.11
	Field 2	NA	NA	NA	NA	NA
	Field 3	0.01	92.57	0.039	2.929	1.534
	Field 4	NA	NA	NA	NA	NA